PHYSICAL REVIEW D **96,** 103021 (2017)

Cosmic rays, antihelium, and an old navy spotlight

Kfir Blum,[1,*] Kenny Chun Yu Ng,[1,†] Ryosuke Sato,[1,‡] and Masahiro Takimoto[1,2,§]

[1]*Department of Particle Physics & Astrophysics, Weizmann Institute of Science, P.O. Box 26, Rehovot 7610001, Israel*

[2]*Theory Center, KEK, 1-1 Oho, Tsukuba, Ibaraki 305-0801, Japan*

(Received 21 April 2017; revised manuscript received 5 October 2017; published 28 November 2017)

Cosmic-ray antideuterium and antihelium have long been suggested as probes of dark matter, as their secondary astrophysical production was thought extremely scarce. But how does one actually predict the secondary flux? Antinuclei are dominantly produced in pp collisions, where laboratory cross section data are lacking. We make a new attempt at tackling this problem by appealing to a scaling law of nuclear coalescence with the physical volume of the hadronic emission region. The same volume is probed by Hanbury Brown–Twiss (HBT) two-particle correlations. We demonstrate the consistency of the scaling law with systems ranging from central and off-axis AA collisions to pA collisions, spanning 3 orders of magnitude in coalescence yield. Extending the volume scaling to the pp system, HBT data allow us to make a new estimate of coalescence that we test against preliminary ALICE pp data. For antihelium the resulting cross section is 1 or 2 orders of magnitude higher than most earlier estimates. The astrophysical secondary flux of antihelium could be within reach of a five-year exposure of AMS02.

DOI: 10.1103/PhysRevD.96.103021

I. INTRODUCTION

Composite cosmic-ray (CR) antinuclei like antideuterium ($\bar{d}$) and antihelium ($\overline{^3\mathrm{He}}$) have long been suggested as probes of dark matter [1–11], as their secondary astrophysical production was thought to be negligible [12–16]. But how does one actually predict the secondary flux? Astrophysical antinuclei are dominantly produced in pp collisions, for which laboratory cross section data are scarce or altogether absent.

We make a new attempt at tackling this problem by appealing to a scaling law of nuclear coalescence with the physical volume of the hadronic emission region. The same volume is probed by Hanbury Brown–Twiss (HBT) two-particle correlation measurements [17,18]. A common tool in heavy ion collision studies [19–24], the HBT method owes its acronym to the inventors of intensity interferometry, utilized in the 1950s for the first angular size determination of a star outside the Solar System using two U.S. Navy spotlights as light buckets [25,26]. In this paper we redirect the HBT idea back to astrophysics, this time in connecting accelerator data to antinuclei CRs.

We show that the scaling law applies to systems ranging from central and off-axis AA collisions to pA and pp collisions, spanning 3 orders of magnitude in coalescence yield. Guided by HBT data we make a new estimate of the $pp \to \overline{^3\mathrm{He}}$ cross section that we validate against preliminary ALICE pp data.

Our results for the $\bar{p}, \bar{d}$, and $\overline{^3\mathrm{He}}$ flux are summarized in Fig. 1. The predicted $\overline{^3\mathrm{He}}$ yield is 1–2 orders of magnitude higher than most earlier estimates [12–16], and the flux could reach, within uncertainties, the expected 5-yr 95% C.L. flux upper limit estimated for AMS02 prior to its launch [27].

The outline of the paper is as follows. We begin by calculating the secondary $\bar{p}$ flux, demonstrating along the way that the astrophysical details of CR propagation are

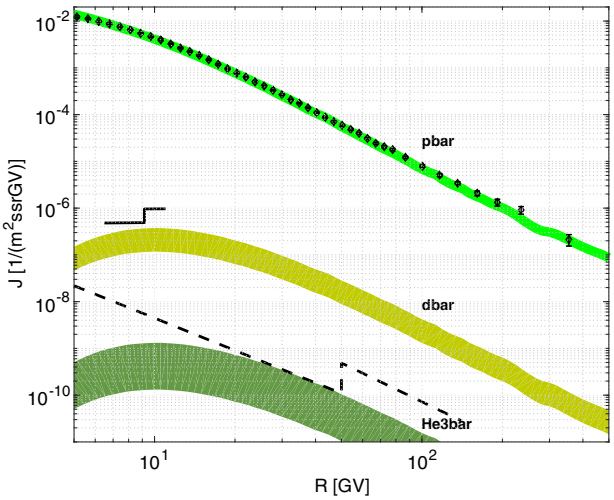

FIG. 1. Predicted flux of $\bar{p}, \bar{d}, \overline{^3\mathrm{He}}$. AMS02 $\bar{p}$ data are taken from Ref. [28]. AMS02 $\bar{d}$ flux sensitivity (5-yr, 95% C.L.) in the kinetic energy range 2.5–4.7 GeV/nuc, as estimated in Ref. [11], is shown by solid line. AMS02 $\overline{^3\mathrm{He}}$ flux sensitivity (5-yr, 95% C.L.), derived from the $\overline{^3\mathrm{He}}$/He estimate of Ref. [27], is shown by dashed line.

*kfir.blum@weizmann.ac.il
†chun-yu.ng@weizmann.ac.il
‡ryosuke.sato@weizmann.ac.il
§masahiro.takimoto@weizmann.ac.il

irrelevant for the calculation of stable, relativistic, secondary CR (anti)nuclei such as $\bar{p}, \bar{d}$, and $\overline{^3\mathrm{He}}$. The challenge, instead, is in computing the production cross sections. Invoking the HBT-coalescence relation, we derive new estimates for the $\bar{d}$ and $\overline{^3\mathrm{He}}$ yield in pp collisions, forming the basis of our results in Fig. 1. Many details are reserved for the Appendixes: Appendix A: Accelerator data analysis; Appendix B: Comparison to previous work; Appendix C: Phase space calculations; Appendix D: Comments on the $\bar{p}p$ secondary source; and Appendix E: Benchmark fragmentation cross sections.

II. CR $\bar{p}$: THE GALAXY IS A FIXED-TARGET EXPERIMENT

CR $\bar{p}, \bar{d}$, and $\overline{^3\mathrm{He}}$ are produced as secondaries in collisions of other CRs, notably protons, with interstellar matter (ISM), notably hydrogen in the Galaxy. While the details of CR propagation are unknown, the confinement in the Galaxy is magnetic, and thus different CR particles that share a common distribution of sources exhibit similar propagation if sampled at the same magnetic rigidity $\mathcal{R} = p/Z$. It is therefore natural to gauge the propagation of CR antinuclei from that of secondary nuclei such as boron (B), formed by fragmentation of heavier CRs. For such secondaries, the ratio of densities of two specie a, b satisfies an approximate empirical relation, valid at relativistic energies ($\mathcal{R} \gtrsim$ few GV) [29–31],

$$\frac{n_a(\mathcal{R})}{n_b(\mathcal{R})} = \frac{Q_a(\mathcal{R})}{Q_b(\mathcal{R})}. \tag{1}$$

Here Q_a denotes the net production of species a per unit ISM column density,

$$Q_a(\mathcal{R}) = \sum_P n_P(\mathcal{R}) \frac{\sigma_{P\to a}(\mathcal{R})}{m} - n_a(\mathcal{R}) \frac{\sigma_a(\mathcal{R})}{m}, \tag{2}$$

where σ_a/m and $\sigma_{P\to a}/m$ are the total inelastic and the partial $P \to a$ cross section per target ISM particle mass m, respectively. These cross sections can (and for $\bar{p}, \bar{d}$, and $\overline{^3\mathrm{He}}$ do) depend on energy. In Eq. (2) we define these cross sections such that the source term $Q_a(\mathcal{R})$ is proportional to the progenitor species density $n_P(\mathcal{R})$ expressed at the same rigidity.

Equation (1) is theoretically natural, in that it is guaranteed to apply if the relative composition of the CRs (not CR intensity, nor target ISM density) in the regions that dominate the spallation is similar to that measured locally at the Solar System [31,32], and as long as no significant energy gain/loss occurs during propagation. Restricting our analysis to $\mathcal{R} \geq 5$ GV, we expect Eq. (1) to be accurate to order 10% or so, as demonstrated by nuclei data [29–31,33].

Equation (1) is useful because we can use the measured flux of B, C, O, p, He, … to predict, e.g., the $\bar{p}$ flux [31,33,34],

$$n_{\bar{p}}(\mathcal{R}) = \frac{n_{\mathrm{B}}(\mathcal{R})}{Q_{\mathrm{B}}(\mathcal{R})} Q_{\bar{p}}(\mathcal{R}). \tag{3}$$

The right-hand side of Eq. (3) is derived from laboratory cross section data and from direct measurements of local CRs, without reference to any detail of propagation.

The quantity

$$X_{\mathrm{esc}}(\mathcal{R}) = \frac{n_{\mathrm{B}}(\mathcal{R})}{Q_{\mathrm{B}}(\mathcal{R})}, \tag{4}$$

known as the CR grammage, measures the column density of ISM traversed by CRs. We combine AMS02 B/C [35] and C/O [36] with heavier CR data from HEAO3 [29] and with laboratory fragmentation cross section data (see e.g. [37]), to derive X_{esc} directly from measurements,

$$X_{\mathrm{esc}} = \frac{(\mathrm{B/C})}{\sum_{\mathrm{P=C,N,O\ldots}} (\mathrm{P/C}) \frac{\sigma_{\mathrm{P}\to\mathrm{B}}}{m} - (\mathrm{B/C}) \frac{\sigma_{\mathrm{B}}}{m}}. \tag{5}$$

Our result for X_{esc} agrees with the power-law approximation derived in Ref. [33] to 20% accuracy.

Now that we have X_{esc}, we use the $\bar{p}$ production and loss cross sections parametrized in [38,39] (applying the correction in [40]) together with measurements of the proton and helium [41,42] flux to calculate $Q_{\bar{p}}$ and apply it in Eq. (3). Solar modulation is included as in [30] with $\Phi = 450$ MV. The result is compared to data in Figs. 1 and 2.

Figures 1 and 2 demonstrate that the $\bar{p}$ flux measured by AMS02 [28] is consistent with secondary production [33]. Beyond this fact, they also demonstrate that—as far as relativistic, stable, secondary nuclei and antinuclei CRs are considered—the Galaxy is essentially a fixed-target

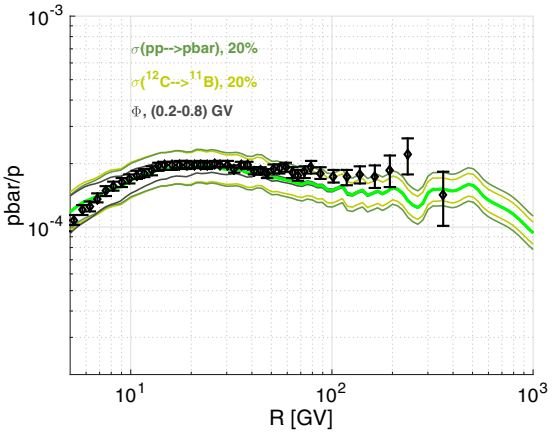

FIG. 2. Observed $\bar{p}/p$ ratio [28] vs the secondary prediction. Wiggles in the theory curve come from our direct data-driven use of the CR grammage, and reflect fluctuations in the AMS02 B/C data [35]. Thick line is the secondary prediction with input cross sections detailed in Appendix E, while thin lines show the response of the prediction for variation in (i) $pp \to \bar{p}$ cross section within ±20%, (ii) fragmentation cross section $p^{12}\mathrm{C} \to {}^{11}\mathrm{B}$ within ±20%, and (iii) variation in the solar modulation parameter in the range $\Phi = (0.2\text{–}0.8)$ GV.

experiment. Having calibrated the setup on one species (B), one can calculate the flux of other secondaries directly from particle physics cross sections. The problem of predicting the antinuclei CR flux is therefore decoupled from the modeling of propagation and is reduced to calculating the relevant cross sections, to which we attend next.

III. CALIBRATING COALESCENCE WITH HBT CORRELATIONS

We use a coalescence ansatz [43–45] relating the formation of composite nucleus product with mass number A to the formation cross section of the nucleon constituents,

$$E_A \frac{dN_A}{d^3p_A} = B_A R(x) \left(E_p \frac{dN_p}{d^3p_p} \right)^A, \tag{6}$$

where $dN_i = d\sigma_i/\sigma$ is the differential yield, σ is the total inelastic cross section, and the constituent momenta are taken at $p_p = p_A/A$.

The factor $R(x)$, with $x = \sqrt{s + A^2 m_p^2 - 2\sqrt{s}\tilde{E}_A}$ and $\tilde{E}_A$ the center of mass product nucleus energy, is a phase space correction that we define as in [46]. This becomes necessary in order to extend the coalescence analysis down to near-threshold collision energies, important for the astrophysics as well as for low energy laboratory data. Details on the derivation of $R(x)$ are given in Appendix C.

B_A, the coalescence factor, needs to be extracted from accelerator data. However, experimental information on $\bar{d}$ and $\overline{^3\mathrm{He}}$ production is scarce and, for the most part, limited to AA or pA collisions. For pp collisions, the most relevant system for CR astrophysics, no quantitative data exist for $pp \to \overline{^3\mathrm{He}}$, and the data for $pp \to \bar{d}$ are sparse.

Faced with this problem, previous estimates [12–16] of the secondary CR $\bar{d}$ and $\overline{^3\mathrm{He}}$ flux made two key simplifying assumptions:

(1) Coalescence parameters used to fit $pp \to \bar{d}$ data were translated directly to $pp \to \overline{^3\mathrm{He}}$. More precisely, the coalescence factor B_A was converted to a coalescence momentum p_c, via

$$\frac{A}{m_p^{A-1}} \left(\frac{4\pi}{3} p_c^3 \right)^{A-1} = B_A. \tag{7}$$

The value of p_c found from $pp \to \bar{d}$ accelerator data was then assumed to describe $pp \to \overline{^3\mathrm{He}}$.

(2) The same coalescence momentum was sometimes assumed to describe both $pA \to \bar{d}$ and $pp \to \bar{d}$.

In what follows we give theoretical and empirical evidence, suggesting that both assumptions may be incorrect. To do this, we make an excursion into the physics of coalescence.

The role of the factor B_A is to capture the probability for A nucleons produced in a collision to merge into a composite nucleus. It is natural for the merger probability to scale as [47–49]

$$B_A \propto V^{1-A}, \tag{8}$$

where V is the characteristic volume of the hadronic emission region. A model of coalescence that realizes the scaling of Eq. (8) was presented in Ref. [17]. A key observation in [17] is that the same hadronic emission volume is probed by HBT two-particle correlation measurements [18]. Both HBT data and nuclear yield measurements are available for AA and pA systems, allowing a test of Eq. (8).

Reference [17] proposed the following formula for the coalescence factor:

$$B_3 = \frac{(2\pi)^3}{4\sqrt{3}} \langle C_3 \rangle (m_t R_1 R_2 R_3)^{-2}. \tag{9}$$

Here, m_t is the transverse mass and R_i are the m_t-dependent HBT scales characterizing the collision. For concreteness we focus on $A = 3$, but the treatment of $A = 2$ is analogous. The quantity $\langle C_3 \rangle$ expresses the finite support of the ^{3}He wave function. It may be estimated via

$$\langle C_3 \rangle \approx \Pi_{i=1,2,3} \left(1 + \frac{b_3^2}{4R_i^2} \right)^{-1}, \tag{10}$$

where $b_3 \approx 1.75$ fm is the ^{3}He nucleus size. For $p_t \lesssim 1$ GeV, setting $R_i \approx R$, we have

$$\frac{B_3}{\mathrm{GeV}^4} \approx 0.0024 \left(\left(\frac{R(p_t)}{1\ \mathrm{fm}} \right)^2 + 0.8 \left(\frac{b_3}{1.75\ \mathrm{fm}} \right)^2 \right)^{-3}. \tag{11}$$

The extension to deuterium, with nucleus size $b_2 = 3.2$ fm, is given by

$$\frac{B_2}{\mathrm{GeV}^2} \approx 0.068 \left(\left(\frac{R(p_t)}{1\ \mathrm{fm}} \right)^2 + 2.6 \left(\frac{b_2}{3.2\ \mathrm{fm}} \right)^2 \right)^{-\frac{3}{2}}. \tag{12}$$

The coalescence factor in AA, pA, and pp collisions, presented with respect to the HBT scale deduced for the same systems, is shown in Fig. 3. The data analysis entering into making the plot is summarized in Appendix A. The data are consistent with Eqs. (11) (bottom panel) and (12) (top panel), albeit with large uncertainty.

HBT data for pp collisions [19,20,50] suggest R in the range 0.5–1.2 fm, indicated by letters in both panels of Fig. 3. For $pp \to \bar{d}$, direct measurements from the ISR [51–53] give

$$B_2^{(pp)} = (0.75\text{–}2.4) \times 10^{-2}\ \mathrm{GeV}^2. \tag{13}$$

As seen in the top panel of Fig. 3, this result is consistent with the intersect of Eq. (12) with the specified range of R. (As done in Refs. [13–15], we discard here the high-p_t data from Serpukhov [54] and only show it in Fig. 3 for completeness. Details can be found in Appendix A.)

For $pp \to \overline{^3\mathrm{He}}$ we do not have direct experimental information. We therefore extract a rough prediction of

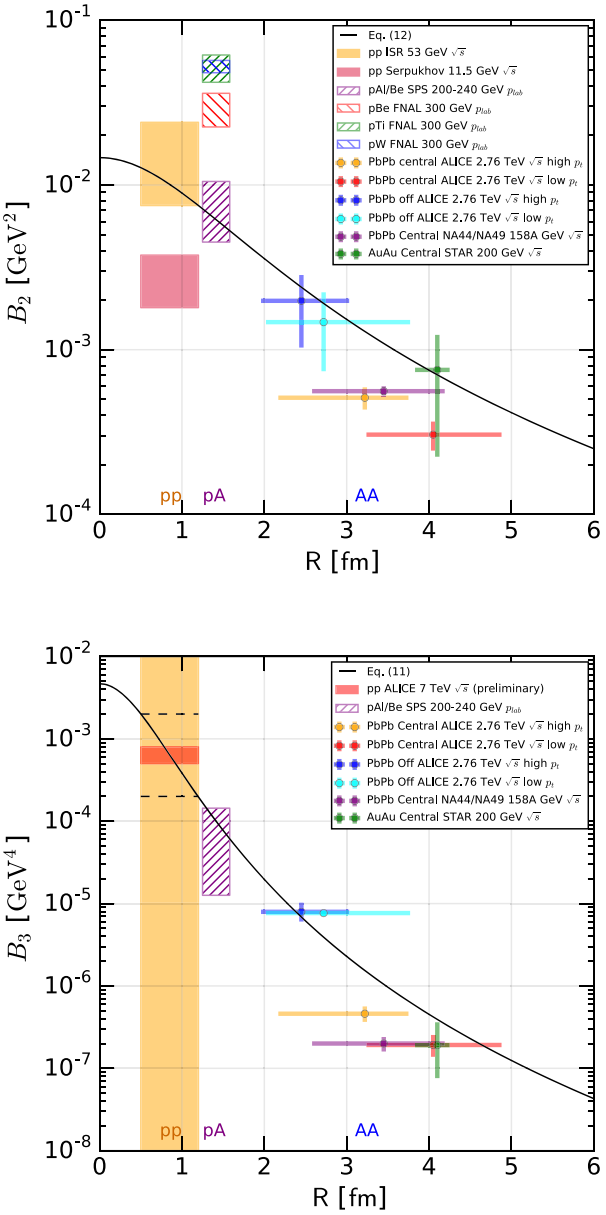

FIG. 3. Coalescence factor B_2 (top) and B_3 (bottom) vs HBT radius. The prediction of Eqs. (11) and (12) is shown as a solid line. Details of the data analysis are given in Appendix A. (Boxes denote systems for which the coalescence factor and the HBT radius are taken from different data sets.)

B_3, by taking the intersect of Eq. (11) with the two ends of the relevant range for R. This gives the following order of magnitude estimate:

$$B_3^{(pp)} = (2\text{–}20) \times 10^{-4}\ \text{GeV}^4 \quad \text{(HBT-based)}, \qquad (14)$$

marked by the two horizontal dashed lines in the bottom panel of Fig. 3.

Results from the ALICE experiment allow us to make a preliminary test of Eq. (14). Reference [55] reported 20 $\overline{^3\text{He}}$ and 20 $\bar{\text{t}}$ in the ALICE pp $\sqrt{s} = 7$ TeV run, corresponding

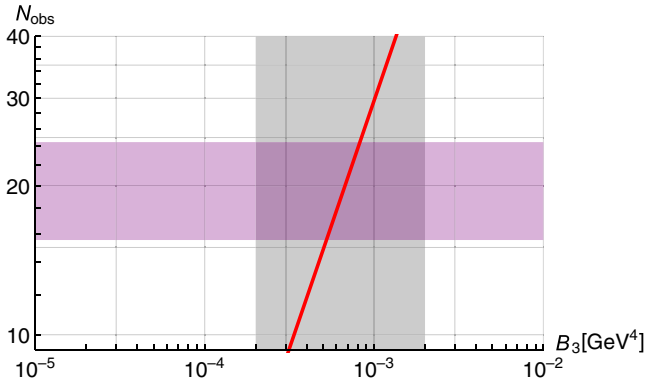

FIG. 4. Analysis of ALICE pp data [55,56]. The number of observed $\overline{^3\text{He}}$ events is shown as a horizontal band with the 1σ Poisson range. Equation (14) is shown by the vertical band. The expected number of events as a function of B_3, imposing the kinematical cuts and efficiency reported for the analysis, is shown by the red line.

to luminosity $\mathcal{L} \approx 2.2$ nb^{-1} with a pseudorapidity cut $|\eta| < 0.9$ and with no further p_t cut.[1] The p_t-dependent efficiency for $\overline{^3\text{He}}$ detection was given in [56]. In Fig. 4 we use these parameters to calculate the expected number of $\overline{^3\text{He}}$ or $\bar{\text{t}}$ events and compare with data. The result supports a coalescence factor $B_3^{(pp)} \approx (5\text{–}8) \times 10^{-4}$ GeV^4, in agreement with Eq. (14). A dedicated analysis by the ALICE Collaboration is highly motivated.

IV. CR ANTIHELIUM

Two channels produce a final state $\overline{^3\text{He}}$: direct $pp \to \overline{^3\text{He}}$ and $pp \to \bar{\text{t}}$ with subsequent decay $\bar{\text{t}} \to \overline{^3\text{He}}$. The first channel should suffer some Coulomb suppression with a Gamow factor that can be estimated by $f_{\text{coul}} \sim e^{-\frac{\pi a m_p}{p_c}}$. Equation (14) suggests $p_c \sim 0.1\text{–}0.2$ GeV, leading to $f_{\text{coul}} \sim 0.8\text{–}0.9$. This is supported by experimental results on the relative yield $^3\text{He}/\text{t}$ [55–57] that are consistent with $f_{\text{coul}} \sim 1$. (Reference [58] reported $\overline{^3\text{He}}/\bar{\text{t}} < 1$; however, the $^3\text{He}/\text{t}$ data from the same publication show an opposite trend, $^3\text{He}/\text{t} \geq 1$.) In what follows, for concreteness we focus on $pp \to \bar{\text{t}}$ but we include a factor of 2 increased yield from the direct $pp \to \overline{^3\text{He}}$ channel.

Combining Eq. (14) with the $pp \to \bar{p}$ production cross section[2] [38,39], we use Eq. (6) to obtain the differential cross section $E_{\bar{\text{t}}} \frac{d\sigma_{pp\to\bar{\text{t}}}}{d^3 p_{\bar{\text{t}}}} = \sigma_{pp} E_{\bar{\text{t}}} \frac{dN_{\bar{\text{t}}}}{d^3 p_{\bar{\text{t}}}}$, where σ_{pp} is the total

[1]We thank Natasha Sharma for clarifying the experimental procedure.

[2]A 19% hyperon contribution to the $\bar{p}$ cross section [59] is subtracted, assuming that coalescence feeds only on prompt $\bar{p}$ and neglecting the contribution from $\overline{^3_\Lambda\text{H}}$ decay.

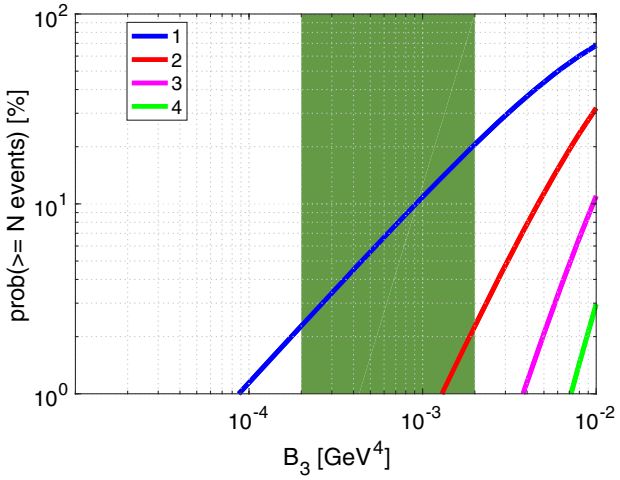

FIG. 5. Poisson probability for detecting $N \geq 1, 2, 3, 4$ $\overline{^3\mathrm{He}}$ events in a 5-yr analysis of AMS02, assuming the same exposure as in the $\bar{p}$ analysis [28]. Equation (14) is shown as a green band.

inelastic pp cross section [60,61]. The effective production cross section to be used in Eq. (2) is then

$$\sigma_{pp\to\overline{^3\mathrm{He}}}(\mathcal{R}) = 2\int_{\epsilon}^{\infty} d\epsilon_p \frac{n_p(\epsilon_p)}{n_p(\mathcal{R})} \frac{d\sigma_{pp\to\bar{\mathrm{t}}}(\epsilon_p,\epsilon)}{d\epsilon}, \quad (15)$$

where

$$\frac{d\sigma_{pp\to\bar{\mathrm{t}}}(\epsilon_p,\epsilon_{\bar{\mathrm{t}}})}{d\epsilon_{\bar{\mathrm{t}}}} = 2\pi p_{\bar{\mathrm{t}}} \int dc_\theta \left(\epsilon_{\bar{\mathrm{t}}} \frac{d\sigma_{pp\to\bar{\mathrm{t}}}}{d^3p_{\bar{\mathrm{t}}}}\right). \quad (16)$$

The final state rigidity and energy are related by $4\mathcal{R}^2 = \epsilon^2 - 9m_p^2$. For the inelastic cross section of $\overline{^3\mathrm{He}}$, entering the loss term in Eq. (2), we use the $\bar{p}$ cross section [38] multiplied by 3.

The resulting $\overline{^3\mathrm{He}}$ flux is plotted in Fig. 1. A prelaunch estimate of the 18 yr 95% C.L. $\overline{^3\mathrm{He}}$ flux upper limit accessible with AMS02 was given in Ref. [27] in terms of the $\overline{^3\mathrm{He}}/\mathrm{He}$ flux ratio. In Fig. 1, in a dashed line, we plot this expected upper limit sensitivity, scaled to 5-yr exposure and multiplied by the observed He flux [42]. We learn that AMS02 may indeed detect secondary $\overline{^3\mathrm{He}}$ in a 5-yr analysis. To further quantify this result, in Fig. 5 we show the Poisson probability for a 5-yr analysis of AMS02 to detect $N \geq 1, 2, 3, 4$ $\overline{^3\mathrm{He}}$ events. The calculation assumes an $\overline{^3\mathrm{He}}$ analysis with the same exposure as the 5-yr $\bar{p}$ analysis of [28].

V. CR ANTIDEUTERIUM

The $\bar{d}$ analysis is analogous to that of $\overline{^3\mathrm{He}}$. The $\bar{d}$ flux is plotted in Fig. 1, for the range of B_2 given in Eq. (13). AMS02 5-yr 95% C.L. $\bar{d}$ flux sensitivity in the kinetic energy range 2.5–4.7 GeV/nuc, estimated in Ref. [11], is shown by solid lines.

VI. SUMMARY

We calculate the flux of secondary cosmic ray $\bar{p}$, $\bar{d}$, and $\overline{^3\mathrm{He}}$. Propagation details are irrelevant to the calculation as long as consistent input data, notably B/C and proton flux, are used to calibrate it. The challenge is in deriving the correct production cross section in pp collisions, the dominant astrophysical source, for which accelerator data are scarce.

Using a scaling law of coalescence with HBT data we derive a novel estimate of the yield of $\overline{^3\mathrm{He}}$ in pp collisions. Our results are consistent with preliminary pp data from ALICE, motivating a dedicated analysis of $B_3^{(pp)}$ by the collaboration itself. Direct $\bar{d}$ data in pp collisions are also consistent with the HBT scaling.

Our prediction for the $pp \to \overline{^3\mathrm{He}}$ cross section is larger by 1–2 orders of magnitude compared to most previous estimates in the literature. The astrophysical secondary flux of $\overline{^3\mathrm{He}}$ is potentially within reach of a five-year exposure of AMS02.

ACKNOWLEDGMENTS

We thank Ulrich W. Heinz and Yosef Nir for reading a draft version of this work, Urs Wiedemann for useful discussions, and Andrei Kounine and Natasha Sharma for clarifying experimental details pertaining to AMS02 and ALICE analyses. This research is supported by the I-CORE program of the Planning and Budgeting Committee and the Israel Science Foundation (Grant No. 1937/12). The work of M. T. is supported by the JSPS Research Fellowship for Young Scientists. K. B. is supported by Grant No. 1507/16 from the Israel Science Foundation and is incumbent of the Dewey David Stone and Harry Levine career development chair.

APPENDIX A: ACCELERATOR DATA FOR NUCLEAR YIELD AND HBT RADIUS

The accelerator data analysis reported in Fig. 3 is summarized below. In all analyses, systematic uncertainties are important, related to the use of imperfect $pp \to \bar{p}$ (and, where required, $pp \to \pi$) cross section parametrization, to the treatment of threshold effects, and in some cases to the lack of complete information from the experiments. We do not attempt statistical fits but merely compare the data with Eq. (6) to extract estimates of B_2 and B_3.

We consider only data corresponding to $\bar{d}$, $\overline{^3\mathrm{He}}$, and $\bar{\mathrm{t}}$ production. Low CME data such as [62] (pA) and [63–69] (AA) demonstrate that production of d and ^{3}He necessarily involves additional processes that are different from the strongly inelastic formation of antinuclei that is of interest to us here. In particular, the approximate CME independence of B_2 and B_3 that is found in high CME experiments is broken for nuclei production very near and below threshold (see e.g. Fig. 28 in Ref. [70]).

Before proceeding to details, we note that different data sets probed different kinematical regions, and it is useful to understand which kinematical regions dominate the astrophysical secondary source. A first rule of thumb is that only low-p_t data are directly relevant to the astrophysics. We demonstrate this point by computing the CR flux, restricting the source term to antinucleus p_t larger than 1 GeV. The result is shown in Fig. 6. As can be seen, the antinucleus CR flux receives only a small contribution from the range $p_t > 1$ GeV. Second, in Fig. 7 we plot the contribution to CR flux coming from pp collisions at different ranges of CME.

We turn to Fig. 3. For the HBT radius R:

(i) *pp Avg E766 30 GeV (R)*: Reference [19] reported the averaged pion HBT radius in fixed target pp collisions at the proton momentum of 27.5 GeV. Their analysis indicates $R \simeq 0.8$–1.2 fm.

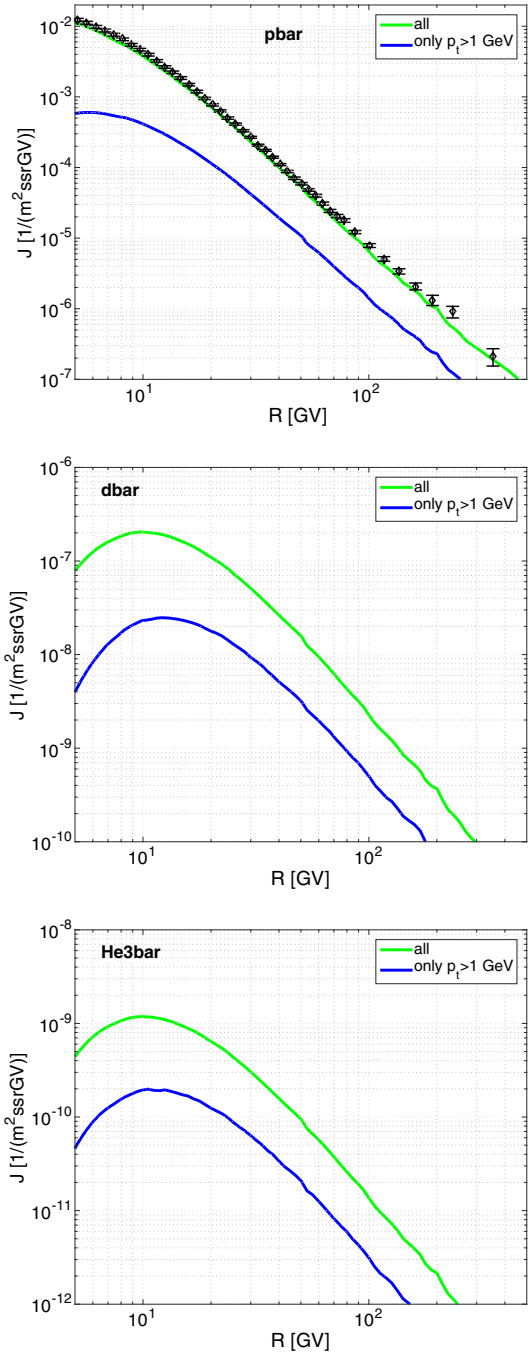

FIG. 6. Contribution of high-p_t region to the secondary astrophysical production of CR antinuclei. $\bar{d}$ and $\overline{^3\mathrm{He}}$ curves use $B_2 = 1.4 \times 10^{-2}$ GeV^2 and $B_3 = 1.9 \times 10^{-3}$ GeV^4, respectively.

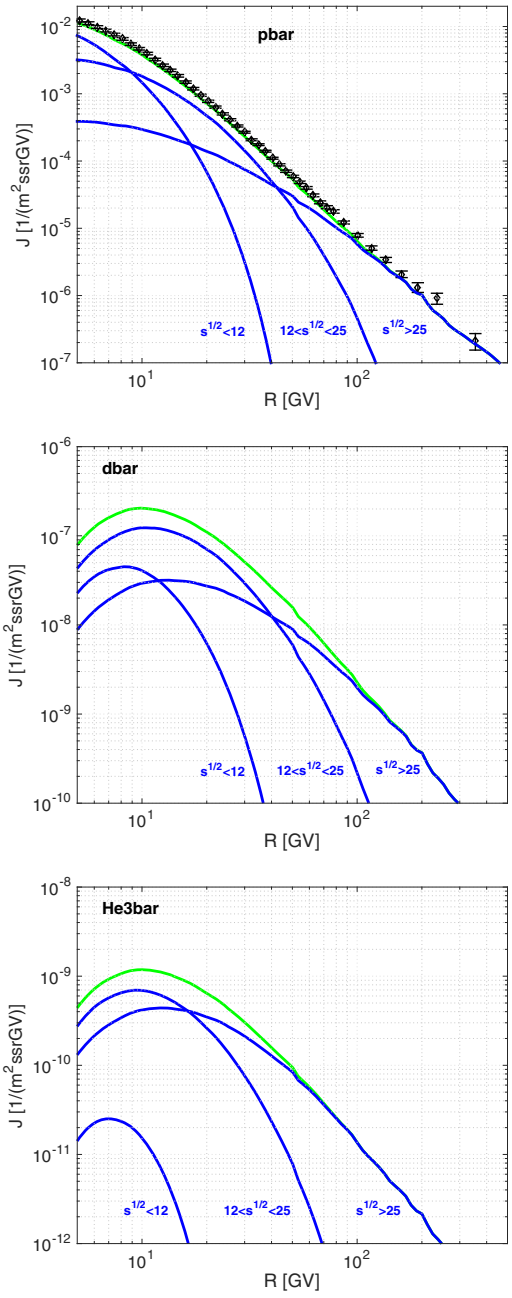

FIG. 7. Contribution of different $\sqrt{s}$ collisions to the secondary astrophysical production of CR antinuclei. $\bar{d}$ and $\overline{^3\mathrm{He}}$ curves use $B_2 = 1.4 \times 10^{-2}$ GeV^2 and $B_3 = 1.9 \times 10^{-3}$ GeV^4, respectively. $\sqrt{s}$ values are in GeV.

(ii) *pp ALICE 7 TeV (R)*: Reference [20] reported the kaon HBT radius in pp collisions at $\sqrt{s} = 7$ TeV. The HBT radius weakly depends on transverse mass m_t for $m_t \gtrsim 1$ GeV. We use the HBT radius data at low charged particle multiplicity and $m_t \simeq 1$ GeV since such a radius is expected to represent the proton HBT radius at lower $\sqrt{s}$. We find $R \approx 0.5$–1.1 fm. In Fig. 3 we join this result to that found above from [19].

(iii) *p*Pb *Avg NA44 450 GeV (R)*: Reference [21] reported the averaged proton HBT radius in the *p*Pb fixed-target experiment at proton momentum of 450 GeV. They give $R = 1.25$–1.58 fm, which we use in Fig. 3 to describe pA systems.

(iv) *PbPb Central/Off ALICE 2.76 TeV with high/low p_t (R)*: Reference [22] reported the antiproton HBT radius in the PbPb collision at $\sqrt{s_{\rm NN}} = 2.76$ TeV. The antiproton HBT radius weakly depends on p_t. We pick up four types of the HBT radius: two centrality classes (central: 0%–10%; and off: 30%–50%) and two transverse momenta (high: $p_t \simeq 1.4$ GeV; and low: $p_t \simeq 0.6$ GeV).

(v) *PbPb Central NA44/NA49 158A GeV (R)*: Reference [23] reported the kaon HBT radius in the central PbPb collision at 158 GeV/nucleon. We use $m_t \simeq 1$ GeV data.

(vi) *AuAu Central STAR 200 GeV (R)*: Reference [24] reported the proton HBT radius in central AuAu collision at $\sqrt{s_{\rm NN}} = 200$ GeV. We use data at $p_t = 0.6$ GeV.

For the derivation of B_2 (upper panel of Fig. 3):

(i) *pp ISR 53 GeV* $[B_2(\bar{d})]$: References [51–53] reported $\bar{d}$ production in pp collisions at $\sqrt{s} = 53$ GeV. Figure 8 summarizes the analysis of [52,53] data, which is the range that we quote in Eq. (13).

The high rapidity data from [51] require care, as our baseline $\bar{p}$ production cross section from Tan and Ng [39] is inaccurate in this kinematical regime. Reference [71] reported $pp \to \bar{p}$ cross sections in the same kinematical regime, where [39] overestimates the data by a factor of 2–3. (That would lead to a factor of 4–9 underestimate in B_2.) The lowest p_t $pp \to \bar{p}$ cross section measurement from [71] is at $\bar{p}$ p_t of 0.15 GeV, allowing us to analyze the highest p_t data point in [51] (out of a grand total of three data points), where the $\bar{d}$ p_t is 0.3 GeV. With this, we find $B_2^{pp}(\bar{d}) = (0.7 - 1.7) \times 10^{-2}$ GeV^2, consistent with Eq. (13).

We do not analyze the ISR data from [72], following the discussion in [73] that pointed out potential inconsistency in the cross section reported for different values of p_t. A quick check, however, suggests that B_2 inferred from [72] is roughly consistent with the other ISR data we analyzed.

(ii) *pp Serpukhov 11.5 GeV* $[B_2(\bar{d})]$: Reference [54] reported $\bar{d}$ production in pp collisions at $\sqrt{s} = 11.5$ GeV. This data set is both low CME and high p_t. The Tan and Ng [39] $pp \to \bar{p}$ cross section fits are consistent (to better than 30%) with the $pp \to \bar{p}$ data reported in [74] for the same setup at $p_t < 0.8$ GeV, but overestimate the data at higher p_t with a factor of 7 discrepancy at $p_t = 2.2$ GeV. (That would lead to a factor of 50 underestimate in B_2.) In Fig. 9 we analyze [54] using $pp \to \bar{p}$ data from [74].

References [13,15] discarded [54] from their analyses. Indeed, our B_2 derived from [54] is significantly lower than that found from the ISR [51–53]. While we do not see any obvious reason to exclude [54], we note that it corresponds to a kinematical regime that is not directly relevant to secondary CR $\bar{d}$ and $\overline{^3\mathrm{He}}$, as seen in Figs. 6 and 7. For that reason we do not include the Serpukhov data in Eq. (13).

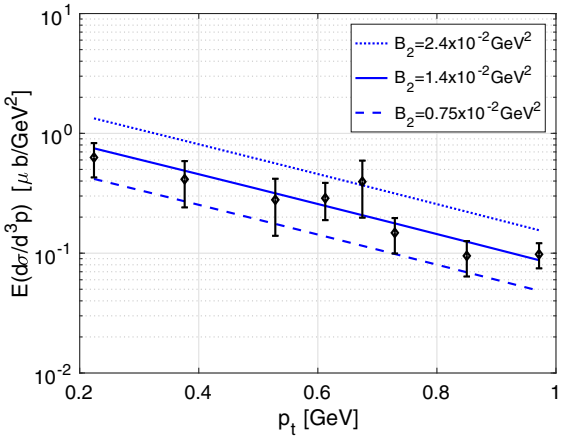

FIG. 8. $B_2^{(pp)}$ from ISR $\sqrt{s} = 53$ GeV $pp \to \bar{d}$ data [52,53], using $\bar{p}$ and π^- cross sections from [39] subtracting a 19% hyperon contribution.

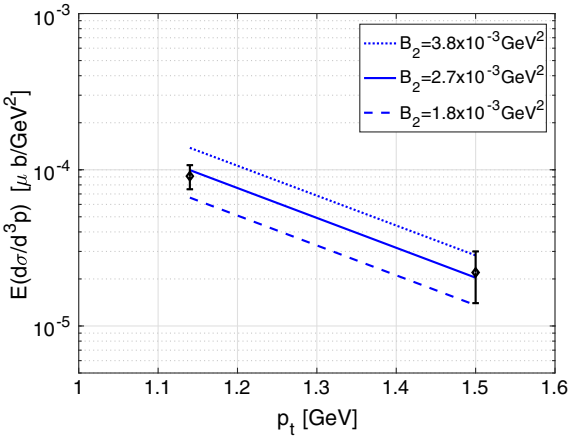

FIG. 9. $B_2^{(pp)}$ from Serpukhov $\sqrt{s} = 11.5$ GeV $pp \to \bar{d}$ data [54], analyzed using $pp \to \bar{p}$ data from [74] subtracting 19% hyperon contribution.

(iii) pAl/Be *SPS 200–240 GeV* [$B_2(\bar{d})$]: CERN SPS pBe and pAl fixed-target $\bar{d}$ data in the forward direction and at proton momentum of 200, 210, 240 GeV were reported in Refs. [58,75]. The nucleon-nucleon CME energy is $\sqrt{s} \approx 19.4$, 19.9, 21.3 GeV. (Note that production of $\bar{d}$ at rest in the center of mass frame corresponds to lab frame $\bar{d}$ momentum $p_{\rm lab} \approx 20$ GeV. Lower/higher $p_{\rm lab}$ means backward/forward momentum in the center of mass frame.) There are no absolute cross section measurements, but rather relative yields, e.g. $\bar{d}/\pi^-$ ratio in given momentum bins. We find that $\bar{p}/\pi^-$ data from [58] are reasonably well described (to ~30%) by the Tan and Ng cross section fits [39]. To analyze the data we multiply the ratio $\bar{d}/\pi^-$ by the $pp \to \pi^-$ cross section and divide by the relevant power of $pp \to \bar{p}$ evaluated at $p_{\bar{p}} = p_{\bar{d}}/2$ to extract B_2. Note that the need to use $pp \to \bar{p}, \pi^-$ as part of the process to extract B_2 (as opposed to deriving B_2 directly from the SPS pA setup, for which, however, we are not given sufficient information) may lead to additional systematic uncertainty. The analysis is summarized in Fig. 10.

(iv) *FNAL* pBe/Ti/W *300 GeV* [$B_2(\bar{d})$]: Reference [76] reported large-angle $\bar{d}$ production in pBe/Ti/W collisions at 300 GeV incident p momentum. The kinematical regime of this data set, $p_t > 2$ GeV, makes a negligible contribution to the astrophysical source, and $\bar{p}/\pi^-$ ratios from this measurement are not reproduced by [39]. Using a combination of $\bar{d}/\bar{p}, \bar{p}/\pi^-$ ratios and π^- production cross sections from the same data set, we derive $B_2^{p\rm Be}(\bar{d}) = (1.5\text{–}2.4) \times 10^{-2}$ GeV^2, $B_2^{p\rm Ti}(\bar{d}) = (2.8\text{–}4.1) \times 10^{-2}$ GeV^2, $B_2^{pW}(\bar{d}) = (3.2\text{–}3.8) \times 10^{-2}$ GeV^2, for $p_t = 2.29$ GeV. These results are then multiplied by a factor of 1.5 to account for hyperon contribution to the $\bar{p}$ cross section in those analyses.

(v) *PbPb Central/Off ALICE 2.76 TeV with high/low* p_t [$B_2(\bar{d}), B_2(d)$]: Reference [56] reported B_2 for d and $\bar{d}$ in PbPb collision at $\sqrt{s_{\rm NN}} = 2.76$ TeV. The data show $B_2(\bar{d}) \approx B_2(d)$, with weak dependence on p_t. We pick up four types of B_2: two centrality classes (central: 0%–10%; and off: 20%–60%) and two transverse momenta (high: $p_t/2 \simeq 1.4$ GeV; and low: $p_t/2 \simeq 0.6$ GeV).

(vi) *PbPb Central NA44/NA49 158A GeV* [$B_2(d)$]: Reference [70] reported B_2 for d in central PbPb collision at 158 GeV/nucleon. B_2 weakly depends on p_t, and we take the $p_t \simeq 0$ data point.

(vii) *AuAu Central STAR 200 GeV* [$B_2(\bar{d})$, $B_2(d)$]: Reference [77] reported B_2 for d and $\bar{d}$ in central AuAu collision at $\sqrt{s_{\rm NN}} = 200$ GeV. The data show $B_2(\bar{d}) \approx B_2(d)$, with weak dependence on p_t. We take the $p_t/2 \simeq 0.8$ GeV data point.

For the derivation of B_3 *(lower panel of Fig. 3):*

(i) pAl/Be *SPS 200–240 GeV* [$B_3(\overline{^3\rm He})$, $B_3(\bar{\rm t})$]: The analysis of the $\overline{^3\rm He}$ and $\bar{\rm t}$ data from Refs. [58,75] is analogous to that described for $\bar{d}$. The systematic uncertainties here are more severe, because the $\bar{p}$ distributions are sampled at lower momentum and because they must be raised to a higher power to extract B_3. Our analysis is summarized in Fig. 11. In quoting the result in Fig. 3 we discard the highest $p_{\rm lab}$ data point.

(ii) *PbPb Central/Off ALICE 2.76 TeV with high/low* p_t [$B_3(\overline{^3\rm He})$, $B_3(^3\rm He)$]: Reference [56] also reported B_3 for both ^{3}He and $\overline{^3\rm He}$ in PbPb collision at $\sqrt{s_{\rm NN}} = 2.76$ TeV. The data show $B_3(\overline{^3\rm He}) \approx B_3(^3\rm He)$ with

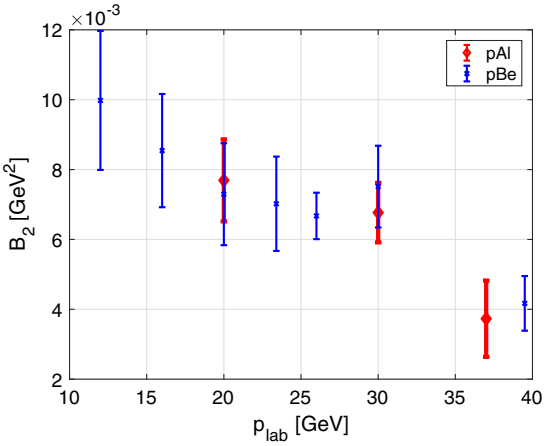

FIG. 10. $B_2^{(pA)}$ from SPS, $p_{\rm lab} = 200$–240 GeV, $\bar{d}$ data [58,75]. We show the inferred value of B_2, with error bars reflecting only the quoted experimental uncertainties on the $\bar{d}/\pi^-$ ratio in the given hadron momentum bins. We use $pp \to \bar{p}, \pi^-$ cross sections from [39] subtracting a 19% hyperon contribution.

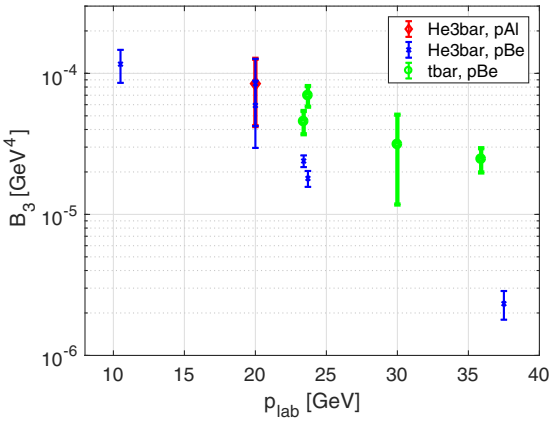

FIG. 11. $B_3^{(pA)}$ from SPS, $p_{\rm lab} = 200$–240 GeV, $\overline{^3\rm He}, \bar{\rm t}$ data [58,75]. We show the inferred value of B_3, with error bars reflecting only the quoted experimental uncertainties on the $\overline{^3\rm He}/\pi^-$ and $\bar{\rm t}/\pi^-$ ratios in the given momentum bins. We use $pp \to \bar{p}, \pi^-$ cross sections from [39] subtracting a 19% hyperon contribution.

weak dependence on p_t. We pick up four types of B_3: two centrality classes (central: 0%–10%; and off: 20%–80%) and two transverse momenta (high: $p_t/3 \simeq 1.4$ GeV; and low: $p_t/3 \simeq 0.8$ GeV).

(iii) *PbPb Central NA44/NA49 158A GeV* [$B^3(^3\mathrm{He})$]: Reference [70] reported B_3 for ^{3}He in central PbPb collision at 158 GeV/nucleon. B_3 weakly depends on p_t and we take the $p_t \simeq 0$ data point.

Reference [78] reported $B_3^{\mathrm{PbPb}}(\overline{^3\mathrm{He}}) = 1^{+2}_{-\infty} \times 10^{-6}$, $B_3^{\mathrm{PbPb}}(^3\mathrm{He}) = 1^{+2}_{-\infty} \times 10^{-5}$, $B_2^{\mathrm{PbPb}}(\bar{d}) = (1-1.5)\times 10^{-3}$, $B_2^{\mathrm{PbPb}}(d) = (0.7-1.1)\times 10^{-3}$. In addition to the PbPb measurements, AA and pA results from other experiments were also summarized, reporting $B_3^{pA} \approx 10^{-4}$, $B_2^{pA} \approx 10^{-2}$, similar for matter and antimatter. In particular, the SPS pAl/Be data of [58] are quoted as $B_3^{pA}(\overline{^3\mathrm{He}}) \approx B_3^{pA}(^3\mathrm{He}) \approx 2 \times 10^{-4}$. However, no derivation is reported, and the latter result—while it agrees with expectations from Eq. (11) and with other data in Fig. 3—does not quite agree with what we find in our own analysis of [58].

(iv) *AuAu Central STAR 200 GeV* [$B_3(\overline{^3\mathrm{He}})$, $B^3(^3\mathrm{He})$]: Reference [77] also reported B_3 for ^{3}He and $\overline{^3\mathrm{He}}$ in central AuAu collision at $\sqrt{s_{\mathrm{NN}}} = 200$ GeV. The data show $B_3(\overline{^3\mathrm{He}}) \approx B_3(^3\mathrm{He})$ with weak dependence on p_t. We take the $p_t/3 \simeq 0.8$ GeV data point.

Finally, we have also analyzed a number of intermediate CME pp and pA experimental results for matter. While these data appear to be generally consistent with the trend for antimatter, we do not add it to Fig. 3, as it may lead to upward bias in B_2 and B_3. Very low CME nuclei production data [62–69] show that matter coalescence (or fragmentation, in this case) contains additional channels beyond those available for antimatter, which may contaminate the intermediate CME regime. For completeness we summarize our results below.

(i) *pp Serpukhov 11.5 GeV* [$B_2(d)$]: Reference [54] also reported the d yield. We analyze the data using $pp \to p$ cross sections from [74]. We find $B_2(d) \sim B_2(\bar{d}) \times 2.2$. As in the $\bar{d}$ data from the same reference, the data correspond to low CME/ high p_t.

(ii) *pAl/Be SPS 200–240 GeV* [$B_2(d)$]: References [58,75] also reported the yield of deuterons. The cross section fits of [39] are inaccurate for $pp \to p$, meaning that we cannot repeat our exercise for the $\bar{d}$ analysis of the same reference. Instead, we use Fig. 4 of [58] to estimate $B_2(d)$, finding $B_2(d) \sim B_2(\bar{d}) \times 2.5$. Note that Fig. 4 of [58] uses a Hagedorn-Ranft model to translate relative hadron yields to the cross section. However, the same model fails to reproduce the relative hadron yields in [58] (see Fig. 2 there). The estimate of $B_2(d)$ derived this way should therefore be taken with caution.

(iii) *FNAL pBe/Ti/W 300 GeV* [$B_2(d)$]: Reference [76] also reported d production. Following a similar prescription as we did for the $\bar{d}$ data, we derive $B_2^{p\mathrm{Be}}(d) = (0.9\text{–}1.3)\times 10^{-2}\,\mathrm{GeV}^2$, $B_2^{p\mathrm{Ti}}(d) = (2\text{–}3)\times 10^{-2}\,\mathrm{GeV}^2$, $B_2^{pW}(d) = (3.0\text{–}3.8)\times 10^{-2}\,\mathrm{GeV}^2$, for $p_t = 2.29$ GeV.

(iv) *pC/Al/Cu/W 50 GeV IHEP-SPIN* [$B_2(d)$]: Reference [79] reported B_2 for d in a collision of 50 GeV proton beam with targets of C, Al, Cu, and W: $B_2 = (1.1\text{–}1.5) \times 10^{-2}$ GeV^2 for $p_t \simeq 1.4$ GeV.

(v) *pC/Al/Cu/W 50 GeV IHEP-SPIN* [$B_3(t)$]: Reference [79] reported B_3 for t in a collision of 50 GeV proton beam with targets of C, Al, Cu, and W, giving $B_3 = (0.8\text{–}1.5) \times 10^{-4}$ GeV^4 for $p_t \simeq 1.8$ GeV.

APPENDIX B: COMPARISON TO PREVIOUS WORK

Our $\bar{d}$ and $\overline{^3\mathrm{He}}$ CR flux prediction is compared to previous work in the top and bottom panels of Fig. 12, respectively. In what follows we present a detailed discussion of this comparison.

Chardonnet et al. [12] found $p_c = 0.058$ GeV for $\bar{d}$, corresponding to $B_2 \approx 1.7 \times 10^{-3}$ GeV^2. The analysis included Serpukhov [54] and ISR [51–53] $pp \to \bar{d}$ data, and was based on $\bar{p}$ cross sections from [39]. The choice of p_c was made to match the Serpukhov data, which yielded the lowest value of p_c (and thus of B_2). We find that fitting B_2 to [54] gives a result that is lower by a factor of ~5 than that needed to fit [52,53].[3] As discussed in Appendix A, we (and similarly [13,15]) use the ISR data [51–53] in Eq. (13), rather than the value found based on the low CME, high-p_t Serpukhov data [54]. To fully compare our $\bar{d}$ flux with [12], we need to modify our phase space factor $R(x)$ to match their different prescription. We show the result in the dotted line in Fig. 12, reproducing the expected factor of 5 between our $\bar{d}$ flux and that of [12].

For $\overline{^3\mathrm{He}}$, Ref. [12] simply used the same value of p_c obtained in the $\bar{d}$ analysis to derive $B_3 \approx 2.3 \times 10^{-6}$ GeV^4. In addition, direct $\overline{^3\mathrm{He}}$ production was neglected and only the $pp \to \bar{\mathrm{t}}$ channel was considered. The net result is a CR $\overline{^3\mathrm{He}}$ flux lower by a factor of ~100 compared to our prediction.

Duperray et al. [13] (following [73]) found $p_c = 0.079$ GeV for $\bar{d}$, corresponding to $B_2 \approx 4.4 \times 10^{-3}$ GeV^2. The analysis collected together pp and pA data sets in a single statistical fit of p_c. As Fig. 3 and Eq. (12) suggest, this could pull the fit artificially to low B_2, if the underlying physics

[3] Our result for B_2 derived from the high rapidity ISR data [51] is higher than that of [12] by a factor of about 7. This is explained by our use of different $pp \to \bar{p}$ cross section fits to analyze this data set. As explained in Appendix A, the Tan and Ng [39] fit overestimates the high rapidity ISR $\bar{p}$ yield [71] by a factor of ~2–3.

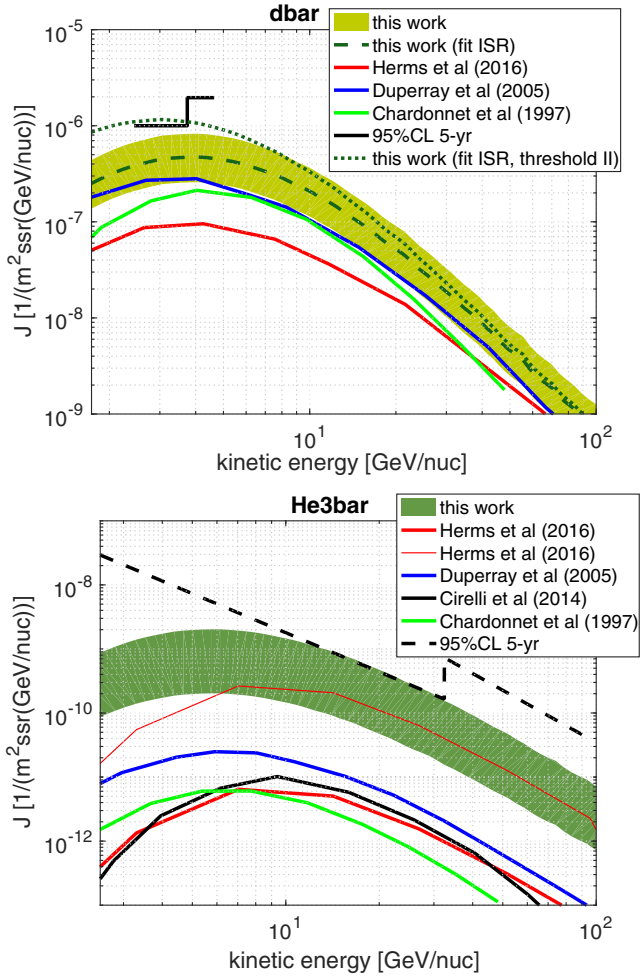

FIG. 12. Comparison to previous work. Top: $\bar{d}$ flux. Bottom: $\overline{^3\mathrm{He}}$ flux. We convert $\bar{d}/p$ and $\overline{^3\mathrm{He}}/p$ ratios from Chardonnet *et al.* [12] using AMS02 p flux [41]. For Duperray *et al.* [13] we take the result including the direct $pp \to \overline{^3\mathrm{He}}$ channel. For Herms *et al.* [16], the $\bar{d}$ prediction is the same as in [14]; for $\overline{^3\mathrm{He}}$ the upper thin line corresponds to their estimate allowing $p_c(\overline{^3\mathrm{He}}) > p_c(\bar{d})$.

satisfies $B_2^{pA} < B_2^{pp}$. In fact, considering the ISR $pp \to \bar{d}$ data [52,53], the global fit of [13] is systematically below the data by a factor of about 2 (see Fig. 1 in [13]). Restoring the factor of 2 gives a result consistent with our Eq. (13) and, given the modest difference in $pp \to \bar{p}$ parametrization, reproduces the difference between our $\bar{d}$ flux and that of [13].

Some more details: for the high rapidity ISR data [51], we reproduce the result of [13] using their $pp \to \bar{p}$ cross section parametrization, but we find that parametrization overestimates the $pp \to \bar{p}$ data of [71] by a factor of ∼2. This may explain why the fit of [13] underestimates [52,53] while at the same time slightly overestimating the highest p_t data point of [51]. The need for a careful treatment of the $pp \to \bar{p}$ cross section in analyzing [51] was also noted by the authors of [73], who, however, extrapolated the $pp \to \bar{p}$ cross section fit derived in [71] to p_t significantly lower than it was made to describe. Moving to pA data, our result for B_2 derived from [58,75] agrees with [13]. The main difference between our $\bar{d}$ analyses, therefore, is that we do not enforce $B_2^{pA} = B_2^{pp}$, such that the low B_2 derived from [58,75] does not control our B_2^{pp} result.

For $\overline{^3\mathrm{He}}$, the $p_c = 0.079$ GeV of [13] translates into $B_3 \approx 1.5 \times 10^{-5}$ GeV^4, which was compared to the sparse data from [58,75]. Our parallel analysis summarized in Fig. 11 gives consistent results. However, as can be made clear by inspection of Fig. 11 here, Fig. 4 in [13], or Table 2 in [58], the sparse data leave room for roughly an order of magnitude of systematic uncertainty in B_3^{pA}. The main difference between our $\overline{^3\mathrm{He}}$ analysis and that in [13] is, therefore, the conclusion: the authors of Ref. [13] made their prediction for B_3^{pp} based on the (poor) B_3^{pA} fit to [58,75], while (i) we allow room for a factor of a few uncertainties in the $\overline{^3\mathrm{He}}$ yield from [58,75], and (ii) we expect $B_3^{pp} > B_3^{pA}$, based on the HBT scaling argument. Finally, another factor of ∼2 enhancing our predicted astrophysical $\overline{^3\mathrm{He}}$ flux compared to that of [13] comes from a difference between our phase space factor $R_5(x)$ and that found by [13], at the relevant range $x \sim 15$–20 GeV. The net outcome is a factor of ∼50 between our $\overline{^3\mathrm{He}}$ flux prediction and that of [13].

Cirelli et al. [15] used PYTHIA 6.4.26 [80] to simulate $\bar{p}$ and $\bar{n}$ production in pp collisions; fitted a coalescence momentum such that the calculation matches the ISR $pp \to \bar{d}$ data from Refs. [52,53]; and then used that coalescence momentum to calculate $\overline{^3\mathrm{He}}$ production. The direct channel $pp \to \overline{^3\mathrm{He}}$ was dropped, and only the $pp \to \bar{\mathrm{t}}$ channel included. The basic building block, $pp \to \bar{p}, \bar{n}$ cross section, was not calibrated in [15] to accelerator data, but simply taken from PYTHIA. We have made a comparison of the $pp \to \bar{p}$ cross section computed in PYTHIA 6.4.26 and by the Tan and Ng [39] parametrization, for the ISR setup [52,53]. The result is shown in Fig. 13. Note that Ref. [15] subtracted the contribution of long-lived $\bar{\Sigma}$ and $\bar{\Lambda}$ baryons from the $\bar{p}$ cross section entering the definition of the coalescence fit. The codes differ by a factor of ∼2 in the relevant low p_t region, with PYTHIA 6.4.26 lying below the Tan and Ng [39] result which, however, does a fairly good job describing low p_t ISR data. The end result is that the $\overline{^3\mathrm{He}}$ flux by [15] is a factor of ∼2 below that of [13], and a factor of ∼100 below ours.

Ibarra and Wild [8,14] did the following exercise. First, in [8] they used $pp \to \bar{p}$ cross sections from PYTHIA 8 [81] to fit a coalescence model to ISR $pp \to \bar{d}$ data [52,53]. Then, in [14], the same p_c was plugged into DPMJET-III [82] to calculate the CR $\bar{d}$ production. This time, an empirical $\sqrt{s}$-dependent correction factor was used to bring the original DPMJET-III $pp \to \bar{p}$ cross section into agreement with experimental data from [83,84] (at the $\sqrt{s} = 53$ GeV of the ISR, for example, DPMJET-III underestimates the $\bar{p}$

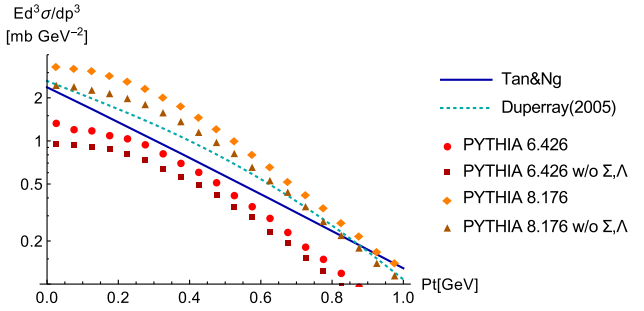

FIG. 13. Comparison of $pp \to \bar{p}$ production cross section parametrization in the ISR setup [52,53]. The authors of Ref. [15] chose to use PYTHIA 6.4.26 to calibrate their $\overline{^3\mathrm{He}}$ production.

multiplicity by a factor of ∼0.7, while at $\sqrt{s} = 6$ GeV [83] it overestimates it by a factor of ∼2).

The end result of this exercise is that the CR $\bar{d}$ flux prediction of [14] is lower than that of [13] by a factor of ∼3 (where we recall that the $\bar{d}$ fit of [13] already underestimates the ISR $pp \to \bar{d}$ data [52,53] by a factor of ∼2); and it is lower than our prediction by a factor of 10.

Herms et al. [16] adopted their $\bar{d}$ production from Ref. [14], discussed above. However, for $\overline{^3\mathrm{He}}$ production, a different set of cross sections is used. We do not enter a detailed comparison to their results. However, we note that following [10] (that focused on a dark matter source for $\overline{^3\mathrm{He}}$), the possibility is entertained that different coalescence momenta could apply to $\bar{d}$ and $\overline{^3\mathrm{He}}$ production, leading to a potential factor of $\gtrsim$10 increase in B_3 compared to what would naively be deduced by using the same p_c; this enhancement is compatible with what we suggest here as our baseline hypothesis.

A general comment should be added in comparing results based on event-by-event Monte Carlo (MC) generators, as done in [8,14–16], to the semianalytic Eq. (6) that we used in the bulk of our analysis. As discussed, for example, in [14], the MC calculation takes into account correlations in the hard process that could modify the coalescence yield near threshold by a factor of order unity. We can quantify the effect by comparing an event-by-event PYTHIA calculation to a calculation based on Eq. (6), where the underlying $\bar{p}$ cross section is taken consistently from the same PYTHIA tune.

Our results are shown in Fig. 14, focusing on $pp \to \bar{d}$ production. The top (bottom) panel corresponds to $\sqrt{s} =$ 53 GeV (20 GeV), respectively. Above threshold—in the top panel—the MC calculation gives identical results to Eq. (6), for both PYTHIA tunes. At lower $\sqrt{s}$, in the bottom panel, the event-by-event PYTHIA 6 calculation falls below Eq. (6) by about a factor of 2, while the PYTHIA 8 event-by-event calculation is consistent with Eq. (6) to about 50%. We conclude that the event-by-event calculation method is in reasonable agreement with Eq. (6), when both methods are based on the same underlying $pp \to \bar{p}$ cross sections.

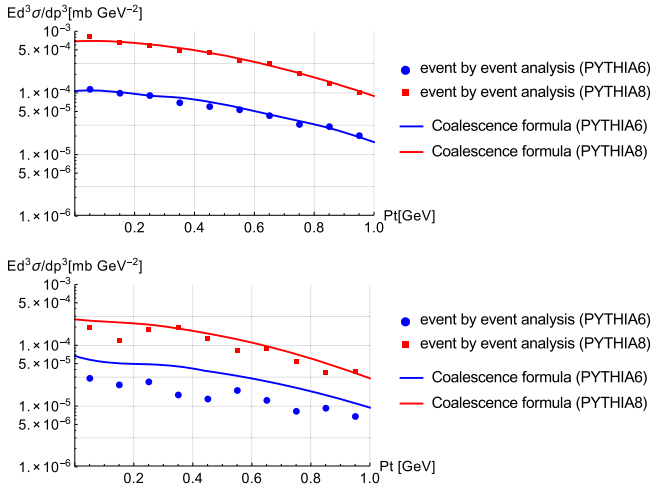

FIG. 14. Comparison of $pp \to \bar{d}$ production cross section, derived by the event-by-event method and by the analytic coalescence formula Eq. (6) using an underlying $pp \to \bar{p}$ cross section from the same PYTHIA tune. We use the PYTHIA 6 and 8 versions of Fig. 13. Top panel: $\sqrt{s} = 53$ GeV. Bottom panel: $\sqrt{s} = 20$ GeV. Both panels use $p_c = 160$ MeV.

Finally, Refs. [12–16] treated CR propagation within specific models, including the leaky-box and homogeneous thin disk + halo diffusion models, while we simply used the secondary relation Eq. (1). As demonstrated by the $\bar{p}$ data in Figs. 1 and 2, apart from some potential $\mathcal{O}(10\%)$ effects that are unimportant in comparison to the particle physics cross section uncertainties, details of propagation are irrelevant to the calculation as long as we keep to the relativistic regime. At low rigidity $\mathcal{R} \lesssim 5$ GV and correspondingly low energies, complications due to the details of propagation in the mildly nonrelativistic regime, solar modulation, energy-dependent fragmentation cross sections entering the grammage analysis, etc., render the analysis complicated and model dependent. For that reason throughout the paper we restricted ourselves to $\mathcal{R} > 5$ GV.

APPENDIX C: PHASE SPACE CORRECTION

Following [46,73], we insert a phase space threshold correction $R(x)$ in Eq. (6), given by the ratio

$$R(x) = \frac{\Phi_N(x, m_p)}{\Phi_N(x, 0)}, \tag{C1}$$

where

$$\Phi_N(x, m) = \left[\Pi_{i=1}^{N} \int \frac{d^3 p_i}{(2\pi)^3 2E_i}\right] (2\pi)^4 \delta^{(4)}\left(\sum_i p_i - P\right) \tag{C2}$$

with $P = (x, \vec{0})$ the phase space of the $N = 2 + A$ mass m nucleons of available CME x that are minimally produced along with a mass number A antinucleus.

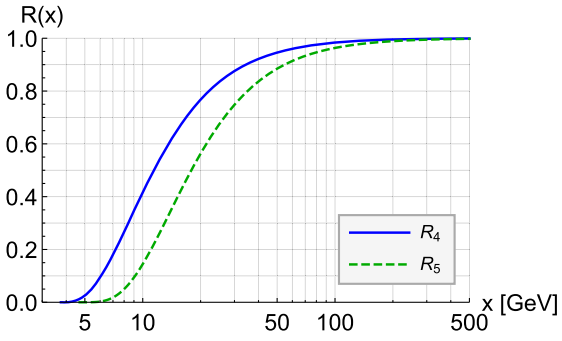

FIG. 15. $R(x)$. For $\bar{d}$ ($\overline{^3\mathrm{He}}$) calculations we use R_4 (R_5).

Our results for $R(x)$ obtained by direct integration differ from the results in [46,73]. For reference we plot our result for $R(x)$ in Fig. 15, which can be directly compared to plots in [46,73]. To judge the numerical importance of the correction factor $R(x)$ to the analysis of laboratory data, note that typical kinematics in [58,75] imply $x \sim 15$–20 GeV, while the data in [54] correspond to $x \sim 9$ GeV.

APPENDIX D: THE $\bar{p}p \to \overline{^3\mathrm{He}}$ SOURCE

In the body of the paper we considered $\bar{d}$ and $\overline{^3\mathrm{He}}$ production in pp scattering. However, given the known CR $\bar{p}$ flux, some contribution to the CR $\bar{d}$ and $\overline{^3\mathrm{He}}$ flux should come from $\bar{p}p$ collisions. This source could in principle be important, despite the low $\bar{p}$ flux, if the production cross section of antinuclei is higher by a factor of 10^4 or so compared to the pp cross section.

Light nuclei production in $\bar{p}p$ scattering was studied in Ref. [85] at $\sqrt{s} = 1.8$ TeV. We estimate that the cross section required for $\bar{p}p \to \bar{\mathrm{t}}$ to produce an observable ratio, $\overline{^3\mathrm{He}}/\bar{p} \sim 10^{-5}$, is on the order of $(\frac{d\sigma_{\bar{p}p\to\bar{\mathrm{t}}}}{dy})_{y=0} \sim 1$ μb. The result of [85] was $(\frac{d\sigma_{\bar{p}p\to t}}{dy})_{y=0} \approx 0.8$ μb; on general grounds, the process should satisfy $\sigma_{\bar{p}p\to\bar{\mathrm{t}}} = \sigma_{\bar{p}p\to t}$. This could suggest that the contribution of $\bar{p}p$ collisions to the CR $\overline{^3\mathrm{He}}$ flux is significant. However, the experimental yield for d production reported in [85] was surprisingly close to the t yield, with $\sigma_{\bar{p}p\to d}/\sigma_{\bar{p}p\to t} \sim 3$. This is to be contrasted with an expected $\mathcal{O}(100)$ hierarchy between the $A = 2$ and $A = 3$ cross sections, a cause for concern that some systematic may be at play. For that reason we do not analyze in detail the $\bar{p}p \to t$ data of [85]. Clarifying the validity of the $(\frac{d\sigma_{\bar{p}p\to\bar{\mathrm{t}}}}{dy})_{y=0}$ result of [85], through careful examination of possible systematics by the experimental collaboration, is highly motivated.

TABLE I. Benchmark decayed fragmentation cross sections.

Reaction	Benchmark cross section [mb]
$^{12}\mathrm{C} \to {}^{11}\mathrm{B}$	55
$^{12}\mathrm{C} \to {}^{10}\mathrm{B}$	14
$^{16}\mathrm{O} \to {}^{11}\mathrm{B}$	25
$^{16}\mathrm{O} \to {}^{10}\mathrm{B}$	9
$^{14}\mathrm{N} \to {}^{11}\mathrm{B}$	30
$^{14}\mathrm{N} \to {}^{10}\mathrm{B}$	9
$^{20}\mathrm{Ne} \to {}^{11}\mathrm{B}$	14
$^{20}\mathrm{Ne} \to {}^{10}\mathrm{B}$	2
$^{24}\mathrm{Mg} \to {}^{11}\mathrm{B} + {}^{10}\mathrm{B}$	15

APPENDIX E: INPUT CROSS SECTIONS FOR GRAMMAGE CALCULATION

Our calculation of secondary CR antinuclei relies on experimental data of other secondary and primary CRs, notably the B/C and C/O flux ratios, in order to calibrate out the effect of CR propagation via the CR grammage X_{esc}. In turn, the derivation of X_{esc} via Eqs. (2)–(4) requires knowledge of decayed nuclear fragmentation cross sections. (For a recent collection of experimental references, see [37].) The fragmentation cross section data are typically specified only at low energies, $\lesssim$2–4 GeV/nuc; we extrapolate this information to high energy assuming that the cross sections remain constant. The experimental uncertainty on the most relevant cross sections—the reactions $^{12}\mathrm{C} \to {}^{11}\mathrm{B}$, $^{16}\mathrm{O} \to {}^{11}\mathrm{B}$—is of order 20%. The projectile species included in the calculation and the benchmark cross section values we use are listed in Table I, and refer to fragmentation on the hydrogen target. These values are based on data summarized in Refs. [86–92]. We extend the result to account for He in the ISM, assuming number density $n_{\mathrm{ISM}} = 0.9n_H + 0.1n_{He}$ and using the formula in Ref. [93]. For the total inelastic cross section of B, we use the formula in Ref. [93].

[1] F. Donato, N. Fornengo, and P. Salati, Antideuterons as a signature of supersymmetric dark matter, Phys. Rev. D **62**, 043003 (2000).

[2] H. Baer and S. Profumo, Low energy antideuterons: Shedding light on dark matter, J. Cosmol. Astropart. Phys. 12 (2005) 008.

[3] F. Donato, N. Fornengo, and D. Maurin, Antideuteron fluxes from dark matter annihilation in diffusion models, Phys. Rev. D **78**, 043506 (2008).

[4] C. B. Brauninger and M. Cirelli, Anti-deuterons from heavy dark matter, Phys. Lett. B **678**, 20 (2009).

[5] M. Kadastik, M. Raidal, and A. Strumia, Enhanced anti-deuteron dark matter signal and the implications of PAMELA, Phys. Lett. B **683**, 248 (2010).

[6] Y. Cui, J. D. Mason, and L. Randall, General analysis of antideuteron searches for dark matter, J. High Energy Phys. 11 (2010) 017.

[7] L. A. Dal and M. Kachelriess, Antideuterons from dark matter annihilations and hadronization model dependence, Phys. Rev. D **86**, 103536 (2012).

[8] A. Ibarra and S. Wild, Prospects of antideuteron detection from dark matter annihilations or decays at AMS-02 and GAPS, J. Cosmol. Astropart. Phys. 02 (2013) 021.

[9] N. Fornengo, L. Maccione, and A. Vittino, Dark matter searches with cosmic antideuterons: Status and perspectives, J. Cosmol. Astropart. Phys. 09 (2013) 031.

[10] E. Carlson, A. Coogan, T. Linden, S. Profumo, A. Ibarra, and S. Wild, Antihelium from dark matter, Phys. Rev. D **89**, 076005 (2014).

[11] T. Aramaki *et al.*, Review of the theoretical and experimental status of dark matter identification with cosmic-ray antideuterons, Phys. Rep. **618**, 1 (2016).

[12] P. Chardonnet, J. Orloff, and P. Salati, The production of antimatter in our galaxy, Phys. Lett. B **409**, 313 (1997).

[13] R. Duperray, B. Baret, D. Maurin, G. Boudoul, A. Barrau, L. Derome, K. Protasov, and M. Buenerd, Flux of light antimatter nuclei near Earth, induced by cosmic rays in the Galaxy and in the atmosphere, Phys. Rev. D **71**, 083013 (2005).

[14] A. Ibarra and S. Wild, Determination of the cosmic antideuteron flux in a Monte Carlo approach, Phys. Rev. D **88**, 023014 (2013).

[15] M. Cirelli, N. Fornengo, M. Taoso, and A. Vittino, Antihelium from dark matter annihilations, J. High Energy Phys. 08 (2014) 009.

[16] J. Herms, A. Ibarra, A. Vittino, and S. Wild, Antideuterons in cosmic rays: Sources and discovery potential, J. Cosmol. Astropart. Phys. 02 (2017) 018.

[17] R. Scheibl and U. W. Heinz, Coalescence and flow in ultrarelativistic heavy ion collisions, Phys. Rev. C **59**, 1585 (1999).

[18] M. A. Lisa, S. Pratt, R. Soltz, and U. Wiedemann, Femtoscopy in relativistic heavy ion collisions, Annu. Rev. Nucl. Part. Sci. **55**, 357 (2005).

[19] J. Uribe *et al.* (BNL-E766 Collaboration), Pion pion correlations at low relative momentum produced in pp collisions at 27.5-GeV/c, Phys. Rev. D **49**, 4373 (1994).

[20] L. V. Malinina (ALICE Collaboration), Kaon femtoscopy of Pb-Pb and pp collisions at the LHC with the ALICE experiment, in Proceedings, 2nd International Conference on New Frontiers in Physics (ICNFP 2013): Kolymbari, Crete, Greece, 2013 (2013).

[21] H. Boggild *et al.* (NA44 Collaboration), Two proton correlations near mid-rapidity in p + Pb S + Pb collisions at the CERN SPS, Phys. Lett. B **458**, 181 (1999).

[22] J. Adam *et al.* (ALICE Collaboration), One-dimensional pion, kaon, and proton femtoscopy in Pb-Pb collisions at $\sqrt{s_{\mathrm{NN}}} = 2.76$ TeV, Phys. Rev. C **92**, 054908 (2015).

[23] I. G. Bearden *et al.* (NA44 Collaboration), Two Kaon Correlations in Central Pb + Pb Collisions at 158 A GeV/c, Phys. Rev. Lett. **87**, 112301 (2001).

[24] Z. Chajecki (STAR Collaboration), Identical particle correlations in STAR, Nucl. Phys. **A774**, 599 (2006).

[25] R. H. Brown and R. Q. Twiss, Correlation between photons in two coherent beams of light, Nature (London) **177**, 27 (1956).

[26] R. Hanbury Brown and R. Q. Twiss, A test of a new type of stellar interferometer on Sirius, Nature (London) **178**, 1046 (1956).

[27] A. Kounine (AMS Collaboration), AMS experiment on the International Space Station, in *Proceedings, 32nd International Cosmic Ray Conference (ICRC 2011): Beijing, China, 2011*, Vol. X, p. 5.

[28] M. Aguilar *et al.* (AMS Collaboration), Antiproton Flux, Antiproton-to-Proton Flux Ratio, and Properties of Elementary Particle Fluxes in Primary Cosmic Rays Measured with the Alpha Magnetic Spectrometer on the International Space Station, Phys. Rev. Lett. **117**, 091103 (2016).

[29] J. Engelmann, P. Ferrando, A. Soutoul, P. Goret, and E. Juliusson, Charge composition and energy spectra of cosmic-ray for elements from Be to NI: Results from HEAO-3-C2, Astron. Astrophys. **233**, 96 (1990).

[30] W. R. Webber, F. B. McDonald, and A. Lukasiak, Voyager 2 measurements in the outer heliosphere of the energy spectra of cosmic-ray nuclei from less than 100 MeV nucleon^{-1} to more than 1.0 GeV nucleon^{-1}, Astrophys. J. **599**, 582 (2003).

[31] B. Katz, K. Blum, J. Morag, and E. Waxman, What can we really learn from positron flux "anomalies"?, Mon. Not. R. Astron. Soc. **405**, 1458 (2010).

[32] V. A. Dogiel, V. S. Berezinsky, S. V. Bulanov, and V. S. Ptuskin, *Astrophysics of Cosmic Rays* (North-Holland, Amsterdam, 1990).

[33] K. Blum, B. Katz, and E. Waxman, AMS-02 Results Support the Secondary Origin of Cosmic Ray Positrons, Phys. Rev. Lett. **111**, 211101 (2013).

[34] T. K. Gaisser and R. K. Schaefer, Cosmic-ray secondary antiprotons: A closer look, Astrophys. J. **394**, 174 (1992).

[35] M. Aguilar *et al.* (AMS Collaboration), Precision Measurement of the Boron to Carbon Flux Ratio in Cosmic Rays from 1.9 GV to 2.6 TV with the Alpha Magnetic Spectrometer on the International Space Station, Phys. Rev. Lett. **117**, 231102 (2016).

[36] S. Ting, The first five years of the alpha magnetic spectrometer on the International Space Station, CERN, 2016, https://indico.cern.ch/event/592392/.

[37] N. Tomassetti, Examination of uncertainties in nuclear data for cosmic ray physics with the AMS experiment, Phys. Rev. C **92**, 045808 (2015).

[38] L. C. Tan and L. K. Ng, Calculation of the equilibrium antiproton spectrum, J. Phys. G **9**, 227 (1983).
[39] L. C. Tan and L. K. Ng, Parametrisation of hadron inclusive cross sections in p-p collisions extended to very low energies, J. Phys. G **9**, 1289 (1983).
[40] M. W. Winkler, Cosmic ray antiprotons at high energies, J. Cosmol. Astropart. Phys. 02 (2017) 048.
[41] M. Aguilar *et al.* (AMS Collaboration), Precision Measurement of the Proton Flux in Primary Cosmic Rays from Rigidity 1 GV to 1.8 TV with the Alpha Magnetic Spectrometer on the International Space Station, Phys. Rev. Lett. **114**, 171103 (2015).
[42] M. Aguilar *et al.* (AMS Collaboration), Precision Measurement of the Helium Flux in Primary Cosmic Rays of Rigidities 1.9 GV to 3 TV with the Alpha Magnetic Spectrometer on the International Space Station, Phys. Rev. Lett. **115**, 211101 (2015).
[43] S. T. Butler and C. A. Pearson, Deuterons from high-energy proton bombardment of matter, Phys. Rev. **129**, 836 (1963).
[44] A. Schwarzschild and C. Zupancic, Production of tritons, deuterons, nucleons, and mesons by 30-GeV protons on A-1, Be, and Fe Targets, Phys. Rev. **129**, 854 (1963).
[45] H. H. Gutbrod, A. Sandoval, P. J. Johansen, A. M. Poskanzer, J. Gosset, W. G. Meyer, G. D. Westfall, and R. Stock, Final State Interactions in the Production of Hydrogen and Helium Isotopes by Relativistic Heavy Ions on Uranium, Phys. Rev. Lett. **37**, 667 (1976).
[46] R. P. Duperray, K. V. Protasov, L. Derome, and M. Buenerd, A model for $A = 3$ anti-nuclei production in proton nucleus collisions, Eur. Phys. J. A **18**, 597 (2003).
[47] R. Bond, P. J. Johansen, S. E. Koonin, and S. Garpman, Breakup densities of nuclear fireballs, Phys. Lett. **71B**, 43 (1977).
[48] A. Mekjian, Thermodynamic Model for Composite Particle Emission in Relativistic Heavy Ion Collisions, Phys. Rev. Lett. **38**, 640 (1977).
[49] L. P. Csernai and J. I. Kapusta, Entropy and cluster production in nuclear collisions, Phys. Rep. **131**, 223 (1986).
[50] K. Aamodt *et al.* (ALICE Collaboration), Two-pion Bose-Einstein correlations in pp collisions at $\sqrt{s} = 900$ GeV, Phys. Rev. D **82**, 052001 (2010).
[51] M. Albrow, D. Barber, P. Benz, B. Bošnjaković, J. Brooks, C. Chang, A. Clegg, F. Erné, P. Kooijman, F. Loebinger, N. McCubbin, P. Murphy, A. Rudge, J. Sens, A. Sessoms, J. Singh, and J. Timmer, Search for stable particles of charge ≥ 1 and mass $\geq$ deuteron mass, Nucl. Phys. **B97**, 189 (1975).
[52] B. Alper, H. Bogild, P. Booth, F. Bulos, L. J. Carroll, G. von Dardel, G. Damgaard, B. Duff, F. Heymann, J. N. Jackson, G. Jarlskog, L. Jonsson, A. Klovning, L. Leistam, E. Lillethun, G. Lynch, G. Manning, M. Prentice, D. Quarrie, J. M. Weiss, and British-Scandinavian Collaboration, Large angle production of stable particles heavier than the proton and a search for quarks at the CERN intersecting storage rings, Phys. Lett. **46B**, 265 (1973).
[53] S. Henning *et al.* (British-Scandinavian-MIT Collaboration), Production of deuterons and anti-deuterons in proton proton collisions at the CERN ISR, Lett. Nuovo Cimento Soc. Ital. Fis. **21**, 189 (1978).
[54] V. V. Abramov *et al.*, High p_T deuteron and anti-deuteron production in pp and p a collisions at 70-GeV, Yad. Fiz. **45**, 1362 (1987) [Sov. J. Nucl. Phys. **45**, 845 (1987)].
[55] N. Sharma (ALICE Collaboration), Production of nuclei and antinuclei in pp and Pb-Pb collisions with ALICE at the LHC, J. Phys. G **38**, 124189 (2011).
[56] J. Adam *et al.* (ALICE Collaboration), Production of light nuclei and anti-nuclei in pp and Pb-Pb collisions at energies available at the CERN Large Hadron Collider, Phys. Rev. C **93**, 024917 (2016).
[57] N. Sharma (ALICE Collaboration), Results from (anti-)(hyper-)nuclei production and searches for exotic bound states with ALICE at the LHC, Nucl. Phys. **A956**, 461 (2016).
[58] A. Bussiére, G. Giacomelli, E. Lesquoy, R. Meunier, L. Moscoso, A. Muller, F. Rimondi, S. Zucchelli, and S. Zylberajch, Particle production and search for long-lived particles in 200240 GeV/c proton-nucleon collisions, Nucl. Phys. **B174**, 1 (1980).
[59] K. Blum, R. Sato, and M. Takimoto, e^+ and $\bar{p}$ production in pp collisions and the cosmic-ray $e^+/\bar{p}$ flux ratio, arXiv:1709.04953.
[60] C. Patrignani *et al.* (Particle Data Group), Review of particle physics, Chin. Phys. C **40**, 100001 (2016).
[61] D. A. Fagundes, M. J. Menon, and P. V. R. G. Silva, On the rise of the proton-proton cross-sections at high energies, J. Phys. G **40**, 065005 (2013).
[62] N. Saito *et al.* (E886 Collaboration), Composite particle production in relativistic Au + Pt, Si + Pt, and p + Pt collisions, Phys. Rev. C **49**, 3211 (1994).
[63] S. Nagamiya, M. C. Lemaire, E. Moller, S. Schnetzer, G. Shapiro, H. Steiner, and I. Tanihata, Production of pions and light fragments at large angles in high-energy nuclear collisions, Phys. Rev. C **24**, 971 (1981).
[64] S. Wang *et al.* (EOS Collaboration), Light Fragment Production and Power Law Behavior in Au + Au Collisions, Phys. Rev. Lett. **74**, 2646 (1995).
[65] J. Barrette *et al.* (E814 Collaboration), Production of light nuclei in relativistic heavy ion collisions, Phys. Rev. C **50**, 1077 (1994).
[66] T. A. Armstrong *et al.* (E864 Collaboration), Antideuteron Yield at the AGS and Coalescence Implications, Phys. Rev. Lett. **85**, 2685 (2000).
[67] T. A. Armstrong *et al.* (E864 Collaboration), Measurements of light nuclei production in 11.5-A-GeV/c Au + Pb Collisions, Phys. Rev. C **61**, 064908 (2000).
[68] M. J. Bennett *et al.* (E878 Collaboration), Light nuclei production in relativistic Au + nucleus collisions, Phys. Rev. C **58**, 1155 (1998).
[69] S. Albergo *et al.*, Light nuclei production in heavy ion collisions at relativistic energies, Phys. Rev. C **65**, 034907 (2002).
[70] T. Anticic *et al.* (NA49 Collaboration), Production of deuterium, tritium, and He3 in central Pb + Pb collisions at 20A, 30A, 40A, 80A, and 158A GeV at the CERN Super Proton Synchrotron, Phys. Rev. C **94**, 044906 (2016).
[71] M. G. Albrow *et al.*, The distribution in transverse momentum of 5 GeV/c secondaries produced at 53 GeV in the centre of mass, Phys. Lett. **42B**, 279 (1972).

[72] J. Armitage, P. Benz, G. Bobbink, F. Erné, P. Kooijman, F. Loebinger, A. Macbeth, H. Montgomery, P. Murphy, J. Poorthuis, L. Rabou, A. Rudge, J. Sens, D. Stork, and J. Timmer, Search for new long-lived particles with masses in the range 1.4 to 3.0 GeV, at the CERN ISR, Nucl. Phys. **B150**, 87 (1979).

[73] R. P. Duperray, K. V. Protasov, and A. Yu. Voronin, Antideuteron production in proton proton and proton nucleus collisions, Eur. Phys. J. A **16**, 27 (2003).

[74] V. V. Abramov *et al.*, Hadron production at transverse momenta from 0.5-GeV up to 2.2-GeV/c in proton proton collisions at 70-GeV, Sov. J. Nucl. Phys. **31**, 484 (1980); Nucl. Phys. **B173**, 348 (1980).

[75] W. Bozzoli, A. Bussière, G. Giacomelli, E. Lesquoy, R. Meunier, L. Moscoso, A. Muller, F. Rimondi, and S. Zylberajch, Production of d, t, 3He, d, t and 3He by 200 GeV protons, Nucl. Phys. **B144**, 317 (1978).

[76] J. W. Cronin, H. J. Frisch, M. J. Shochet, J. P. Boymond, R. Mermod, P. A. Piroue, and R. L. Sumner, Production of hadrons with large transverse momentum at 200, 300, and 400 GeV, Phys. Rev. D **11**, 3105 (1975).

[77] H. Liu, Light nuclei production in $\mathrm{Au}+\mathrm{Au}$ 200-GeV collisions at RHIC, Int. J. Mod. Phys. E **16**, 3280 (2007).

[78] S. Kabana *et al.*(the NA52 Collaboration), Recent results from experiment NA52 at the CERN SPS, J. Phys. G **23**, 2135 (1997).

[79] N. N. Antonov *et al.*, Knockout of deuterons and tritons with large transverse momenta in pA collisions involving 50-GeV protons, Pis'ma Zh. Eksp. Teor. Fiz. **104**, 678 (2016) [JETP Lett. **104**, 662 (2016)].

[80] T. Sjostrand, S. Mrenna, and P. Z. Skands, PYTHIA 6.4 physics and manual, J. High Energy Phys. 05 (2006) 026.

[81] T. Sjostrand, S. Mrenna, and P. Z. Skands, A brief introduction to PYTHIA 8.1, Comput. Phys. Commun. **178**, 852 (2008).

[82] S. Roesler, R. Engel, and J. Ranft, The Monte Carlo event generator DPMJET-III, in *Advanced Monte Carlo for Radiation Physics, Particle Transport Simulation and Applications. Proceedings of the MC2000 Conference, Lisbon, Portugal, 2000* (Springer-Verlag, Berlin, 2001), pp. 1033–1038.

[83] J. V. Allaby, F. G. Binon, A. N. Diddens, P. Duteil, A. Klovning, and R. Meunier, CERN Report No. CERN-70-12, 1970.

[84] M. Antinucci, A. Bertin, P. Capiluppi, M. D'Agostino-Bruno, A. M. Rossi, G. Vannini, G. Giacomelli, and A. Bussiere, Multiplicities of charged particles up to ISR energies, Lett. Nuovo Cimento Soc. Ital. Fis. **6**, 121 (1973).

[85] T. Alexopoulos *et al.*, Cross sections for deuterium, tritium, and helium production in pp collisions at $s = 1.8$-TeV, Phys. Rev. D **62**, 072004 (2000).

[86] A. Korejwo, M. Giller, T. Dzikowski, V. V. Perelygin, and A. V. Zarubin, Isotopic cross sections of 12 c fragmentation on hydrogen measured at 1.87 and 2.69 GeV/nucleon, J. Phys. G **28**, 1199 (2002).

[87] A. Korejwo, T. Dzikowski, M. Giller, J. Wdowczyk, V. V. Perelygin, and A. V. Zarubin, The measurement of isotopic cross sections of 12 c beam fragmentation on liquid hydrogen at 3.66 GeV/nucleon, J. Phys. G **26**, 1171 (2000).

[88] D. L. Olson, B. L. Berman, D. E. Greiner, H. H. Heckman, P. J. Lindstrom, and H. J. Crawford, Factorization of fragment-production cross sections in relativistic heavy-ion collisions, Phys. Rev. C **28**, 1602 (1983).

[89] P. A. Benioff, Nuclear reactions of low-z elements with 5.7-beV protons, Phys. Rev. **119**, 316 (1960).

[90] W. R. Webber, J. C. Kish, J. M. Rockstroh, Y. Cassagnou, R. Legrain, A. Soutoul, O. Testard, and C. Tull, Production cross sections of fragments from beams of 400–650 MeV per nucleon 9Be, 11B, 12C, 14N, 15N, 16O, 20Ne, 22Ne, 56Fe, and 58Ni nuclei interacting in a liquid hydrogen target. IIi. Isotopic cross sections of fragments, Astrophys J. **508**, 949 (1998).

[91] R. Silberberg, C. H. Tsao, and A. F. Barghouty, Updated partial cross sections of proton-nucleus reactions, Astrophys. J. **501**, 911 (1998).

[92] C. N. Knott *et al.*, Systematics elemental production cross sections from neon to nickel, Int. Cosmic Ray Conf. **2**, 187 (1993).

[93] P. Ferrando, W. R. Webber, P. Goret, J. C. Kish, D. A. Schrier, A. Soutoul, and O. Testard, Measurement of ^{12}C, ^{16}O, and ^{56}Fe charge changing cross sections in helium at high-energy, comparison with cross sections in hydrogen, and application to cosmic ray propagation, Phys. Rev. C **37**, 1490 (1988).